Quaternary Research (2018), **90**, 26–37.

doi:10.1017/qua.2018.12

Rapid age assessment of glacial landforms in the Pyrenees using Schmidt hammer exposure dating (SHED)

Matt D. Tomkins[a,*], Jason M. Dortch[a,b], Philip D. Hughes[a], Jonny J. Huck[a], Andrew G. Stimson[a], Magali Delmas[c], Marc Calvet[c], Raimon Pallàs[d]

[a]Cryosphere Research at Manchester, Department of Geography, University of Manchester, Manchester M13 9PL, United Kingdom
[b]Kentucky Geological Survey, 228 Mining and Mineral Resources Building, University of Kentucky, Lexington, Kentucky 40506, USA
[c]Université de Perpignan Via-Domitia, UMR 7194 CNRS Histoire Naturelle de l'Homme Préhistorique, 66860 Perpignan Cedex, France
[d]Departament de Dinàmica de la Terra i de l'Oceà, Universitat de Barcelona, 08028 Barcelona, Spain

(Received October 18, 2017; Accepted January 24, 2018)

Abstract

Schmidt hammer (SH) sampling of 54 ^{10}Be-dated granite surfaces from the Pyrenees reveals a clear relationship between exposure and weathering through time ($n = 52$, $R^2 = 0.96$, $P < 0.01$) and permits the use of the SH as a numerical dating tool. To test this ^{10}Be-SH calibration curve, 100 surfaces were sampled from five ice-front positions in the Têt catchment, eastern Pyrenees, with results verified against independent ^{10}Be and ^{14}C ages. Gaussian modelling differentiates Holocene (9.4 ± 0.6 ka), Younger Dryas (12.6 ± 0.9 ka), Oldest Dryas (16.1 ± 0.5 ka), last glacial maximum (LGM; 24.8 ± 0.9 ka) and Würmian maximum ice extent stages (MIE; 40.9 ± 1.1 ka). These data confirm comparable glacier lengths during the LGM and MIE (~300 m difference), in contrast to evidence from the western Pyrenees (≥15 km), reflecting the relative influence of Atlantic and Mediterranean climates. Moreover, Pyrenean glaciers advanced significantly during the LGM, with a local maximum at ~25 ka, driven by growth of the Laurentide Ice Sheet, southward advection of the polar front, and a solar radiation minimum in the Northern Hemisphere. This calibration curve is available online (http://shed.earth) to enable wider application of this method throughout the Pyrenees.

Keywords: Schmidt hammer exposure dating; Pyrenees; Glacier chronology; Geomorphology; Terrestrial cosmogenic nuclide dating; Last glacial maximum

INTRODUCTION

The Quaternary glacial record of the Pyrenees is essential for reconstructing regional paleoclimate and provides crucial information on the response of terrestrial ice masses to variability in the North Atlantic atmosphere-ocean circulation system (Pallàs et al., 2010). However, determining causal links between climate and glacier response is predicated on the development of robust chronological frameworks. Recent advances in terrestrial cosmogenic nuclide (TCN) and optically stimulated luminescence (OSL) dating techniques and their application to glacial and glaciofluvial deposits have helped constrain the chronology of late Pleistocene glaciation (Würmian stage) and in particular the timing of the Würmian maximum ice extent (MIE). ^{10}Be ages from Ariège (Delmas et al., 2011, 2015) and Malniu (Pallàs et al., 2010) show that MIE glaciers in the eastern Pyrenees terminated just downvalley of last glacial maximum (LGM) limits (23.3–27.5 ka; Hughes and Gibbard, 2015). This appears to contrast with glaciers in the western Pyrenees, where LGM glaciers failed to reach MIE limits by ~15 km (Jalut et al., 1992; Calvet et al., 2011; Delmas, 2015), perhaps reflecting the contrasting influence of Atlantic and Mediterranean climates (Delmas et al., 2011). However, this hypothesis is limited by the relative scarcity of geochronological data and the increasing fragmentation of trunk glaciers into isolated ice masses during retreat and downwastage of the Pyrenean ice field. These difficulties, exacerbated by the fragmentary nature of the geomorphological record, preclude straightforward stratigraphic correlation of glacial deposits and have thus far prevented a Pyrenean-scale synthesis of post-Marine Isotope Stage (MIS) 4 glaciation.

TCN dating is well suited to address this knowledge gap as glacial deposits are well preserved in the Pyrenees. However, moraine stabilisation (Hallet and Putkonen, 1994) and

* Corresponding author at: Cryosphere Research at Manchester, Department of Geography, University of Manchester, Manchester M13 9PL, United Kingdom. E-mail address: matthew.tomkins@postgrad.manchester.ac.uk (M.D. Tomkins).

nuclide inheritance (Putkonen and Swanson, 2003) can result in "young" and "old" ages, respectively (Heyman et al., 2011; Murari et al., 2014). The most significant barrier to isolating these ages is the cost of TCN dating, which often precludes high-sample studies and, in turn, prevents statistically robust identification and rejection of erroneous results. Thus, new cost- and time-efficient dating techniques are necessary that complement existing radiometric techniques and can be applied widely to undated glacial landforms. In the British Isles, a clear relationship between TCN exposure ages and Schmidt hammer (SH) rebound values (*R* values) was recorded for 54 dated granite surfaces ($R^2 = 0.94$, $P < 0.01$; 0.8–23.8 ka; Tomkins et al., 2016, 2018) and permits the estimation of exposure time based on surface *R* values. This TCN-SH calibration curve has been applied to glacial landforms in the Mourne Mountains (Barr et al., 2017) and the Lake District (Tomkins et al., 2016), with results consistent with existing radiometric ages (^{10}Be, ^{14}C). However, direct application of this calibration curve to Pyrenean deposits is unsuitable as long-term weathering rates exhibit systematic variability between climatic regimes (Riebe et al., 2004). This variability is likely significant between the temperate-oceanic climate of the British Isles and the comparatively dry, continental Pyrenees. In this article, we develop and verify the first Pyrenean SH exposure dating (SHED) calibration curve and generate new chronological data to constrain the deglacial chronology of Têt glacier, a major outlet of the Pyrenean ice field. These new chronological data are supported by independent ^{10}Be ages, are consistent with previous geomorphological assessments (Delmas et al., 2008), and contribute significantly to our understanding of post–MIS 4 glacier dynamics.

METHODS

Fifty-four TCN-dated granite surfaces from across the Pyrenees were sampled using the N-type SH (Fig. 1, Table 1; Pallàs et al., 2006, 2010; Crest et al., 2017). Sampled surfaces (Fig. 2) include moraine boulders (n = 39) and ice-sculpted bedrock (n = 15) from a range of elevations (981–2817 m) and geomorphological settings. All surfaces were of sufficient size (Sumner and Nel, 2002) and were free of surface discontinuities (Williams and Robinson, 1983) and lichen (Matthews and Owen, 2008). Sampled surfaces were coarse- to medium-grained granite and granodiorite from the Hercynian Axial Zone (Crest et al., 2017). Axial zone granites were uplifted during and after the late Cretaceous following collision of Europe and the Iberian microplate, with deformation ceasing at ~20–25 Ma, followed by post-orogenic uplift over the last ~10 Ma (Gunnell et al., 2009; Ortuño et al., 2013). The predominant style of weathering is subaerial, as evidenced by granular disintegration of the crystalline rock surface (André, 2002). There is no clear variability in grain size or rock composition between sites (Fig. 1B). Thirty *R* values were recorded per surface. This exceeds the recommendation of Niedzielski et al. (2009) of 20 *R* values for granite surfaces (minimum sample size in terms of mean at $\alpha = 0.05$). Carborundum treatment was used to remove surface irregularities prior to testing (Katz et al., 2000; Černá and Engel, 2011; Engel et al., 2011; Viles et al., 2011; Kłapyta, 2013). There is ongoing debate as to whether rock surfaces should be smoothed prior to testing (Moses et al., 2014). However, the data presented in this study indicate that a consistent sampling approach enables age-related information to be retained—that is, recently exposed surfaces

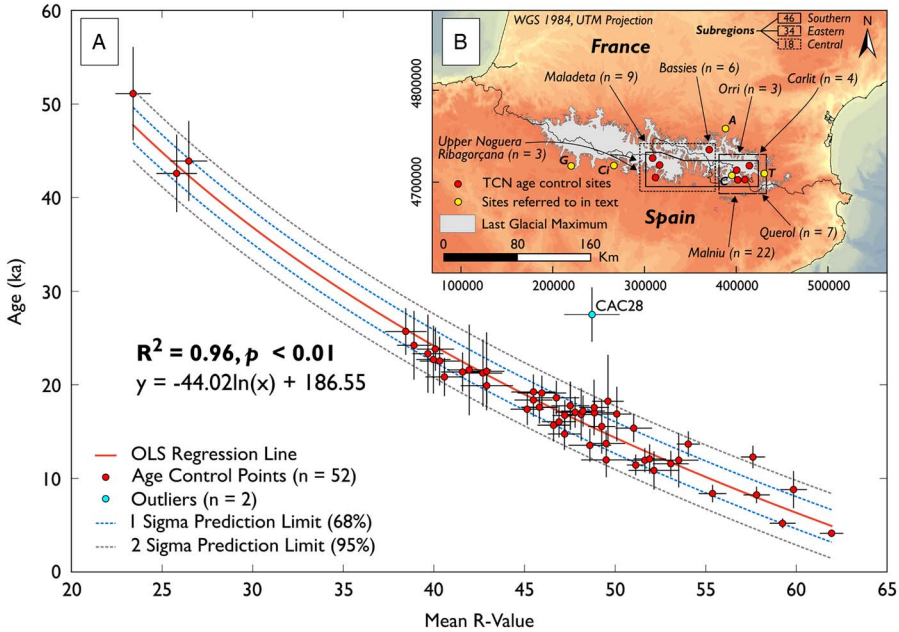

Figure 1. (colour online) Schmidt hammer exposure dating calibration curve for the Pyrenees. (A) Correlation between Schmidt hammer *R* values and terrestrial cosmogenic nuclide (TCN) exposure ages (n = 53). Inherited outlier ICM04 not shown as it is beyond the graph axis (age = 80.7 ± 7.9 ka, *R* value = 24.98 ± 1.17). (B) Map of age control sites, sites referred to in text (A, Ariege; C, Campcardós; Ci, Cinca; G, Gállego; T, Têt), and the last glacial maximum extent after Calvet et al. (2011).

https://doi.org/10.1017/qua.2018.12 Published online by Cambridge University Press

Table 1. Details of ^{10}Be-dated surfaces sampled using the Schmidt hammer.

Sample	Coordinates[a]		Elevation (m)	Type	Subregion[b]	Boulder height (m)	Cirque distance (km)	Mean *R* value	SEM[c]	Age (ka)	1σ (ka)
MA03	306645	4726398	2396	Bedrock	S + C	-	1.7	54.03	0.65	13.67	1.36
MA04	306659	4725978	2560	Boulder	S + C	2	1.4	57.60	0.67	12.29	1.21
MA11	306498	4725387	2789	Bedrock	S + C	-	1	61.93	0.65	4.13	0.41
MA12	306627	4725290	2817	Bedrock	S + C	-	1	59.23	0.71	5.21	0.52
MA07	306901	4725631	2665	Bedrock	S + C	-	1.5	51.13	0.49	11.43	1.12
MA05	306959	4726408	2342	Boulder	S + C	1.5	2.05	57.80	0.73	8.24	0.88
MA06	306991	4726657	2283	Boulder	S + C	2	2.2	49.50	1.04	13.73	1.41
AN02	308872	4726401	2050	Boulder	S + C	1	3.3	48.60	1.18	13.54	1.77
AN01	308669	4726819	2020	Boulder	S + C	1.8	3.9	47.20	0.91	14.74	1.69
STA01	311923	4704290	998	Boulder	S + C	1.2	22	48.84	0.82	17.58	2.98
SMV01	312411	4706093	981	Boulder	S + C	0.5	19.9	59.84	0.74	8.80	1.99
RHL01	316483	4718607	1472	Bedrock	S + C	-	6	49.60	0.87	18.25	4.95
BA15	371797	4735829	1678	Boulder	C	1.7	5.2	46.60	0.89	15.69	1.74
BA16	371426	4736078	1741	Boulder	C	0.7	5	46.90	0.94	16.05	1.69
BA20	369354	4734473	1837	Bedrock	C	-	2.10	51.64	0.95	11.94	1.29
BA19	369354	4734473	1837	Bedrock	C	-	2.1	55.37	0.76	8.38	0.93
BA17	369697	4734705	1885	Boulder	C	0.8	2.6	51.90	0.90	12.07	1.57
BA18	369717	4734785	1890	Boulder	C	0.7	2.7	53.07	0.99	11.57	1.37
FUL03	403443	4707445	1476	Bedrock	S + E	-	10	42.90	0.99	21.45	4.17
LAT01	408106	4702521	1279	Bedrock	S + E	-	17	42.70	1.07	21.26	3.59
YRA-21	408727	4701033	1341	Boulder	S + E	1.4	18.5	39.97	0.94	22.69	3.62
YRA-20	408719	4701031	1349	Boulder	S + E	1	18.5	39.67	0.86	23.32	4.19
YRA-19	408651	4701040	1354	Boulder	S + E	1.8	18.5	38.90	0.94	24.22	3.67
CAC25	414113	4718126	2356	Bedrock	S + E	-	0.6	52.14	1.41	10.85	2.04
CAC26	414113	4718126	2357	Bedrock	S + E	-	0.6	49.51	1.38	11.97	1.85
CAC27	414113	4718126	2360	Bedrock	S + E	-	0.6	53.51	1.09	11.95	2.92
CAC28	414113	4718126	2356	Bedrock	-	-	0.6	48.71	1.53	26.93[d]	2.89
QRS01	406616	4703876	1346	Bedrock	S + E	-	15.1	41.95	1.21	21.59	4.84
ICM01	404800	4702660	1861	Boulder	S + E	2	6.3	23.41	0.98	51.11	4.99
ICM02	404787	4702624	1863	Boulder	S + E	1	6.3	26.48	1.02	43.91	4.28
ICM03	404764	4702592	1863	Boulder	S + E	1.2	6.3	25.81	1.12	42.59	4.15
ICM04	404736	4702569	1864	Boulder	-	1.5	6.3	24.98	1.17	80.73[d]	7.92
OEC5	404606	4702925	1935	Boulder	S + E	2.2	6.3	40.58	1.06	20.84	2.04
OEC4	404545	4702828	1945	Boulder	S + E	2	6.2	45.15	0.92	17.39	1.70
OEC6	404548	4703058	1937	Boulder	S + E	1.6	6.1	45.82	0.98	17.58	1.73
OEC3	404415	4702566	1951	Boulder	S + E	2	6	45.82	1.02	17.61	1.74
OEC2	404329	4702532	1956	Boulder	S + E	1.7	5.9	41.58	1.20	21.37	2.09
OEC1	404402	4702668	1953	Boulder	S + E	1.4	6	40.08	1.03	23.81	2.32
LAF03	402597	4701952	2168	Boulder	S + E	2.2	3.9	45.49	1.22	19.23	1.87
LAF01	402493	4701917	2174	Boulder	S + E	2	3.9	40.32	1.10	22.54	2.63
LAF04	401565	4701602	2213	Boulder	S + E	1	3.2	38.45	1.15	25.69	2.50
OMA04	400874	4702314	2267	Boulder	S + E	1.3	2	45.49	1.05	18.38	1.79
OMA02	400871	4702326	2268	Boulder	S + E	2	2	42.92	1.44	19.91	1.93
OMA03	400877	4702330	2267	Boulder	S + E	2.4	2	46.76	1.26	18.62	1.81
OMA01	400884	4702332	2267	Boulder	S + E	1.9	2	45.95	1.34	19.13	1.86
IMA03	400931	4703060	2287	Boulder	S + E	2.3	1.8	48.86	1.07	17.02	1.66
IMA01	400943	4703050	2289	Boulder	S + E	3	1.8	47.22	0.68	16.72	1.63
IMA02	400924	4703031	2286	Boulder	S + E	3.5	1.8	51.02	1.01	15.37	1.50
IMA04	401069	4703262	2270	Boulder	S + E	3	1.6	47.79	1.09	17.08	1.66
IMA05	401073	4703284	2290	Boulder	S + E	2	1.6	48.22	1.22	17.19	1.67
CPM03	400965	4712601	2032	Boulder	S + E	0.9	3.6	50.09	0.82	16.87	2.91
CPM01	400805	4712550	2039	Boulder	S + E	1.2	3.6	48.12	1.09	16.83	2.81
CPM02	400809	4712566	2038	Boulder	S + E	1.1	3.6	49.26	0.76	15.54	2.90
CAS03	403474	4710840	1681	Bedrock	S + E	-	6.6	47.52	1.05	17.75	2.59

[a]With reference to WGS 1984 31 T.
[b]C, central; E, eastern; S, southern.
[c]SEM, standard error of the mean.
[d]Inherited surface.

https://doi.org/10.1017/qua.2018.12 Published online by Cambridge University Press

Figure 2. (colour online) ^{10}Be-dated surfaces sampled using the Schmidt hammer. Holocene (A), Younger Dryas (B), last glacial maximum (C), and Würmian maximum ice extent (D) dated surfaces from Pallàs et al. (2010) and Crest et al. (2017). Reported ^{10}Be ages were recalibrated using the online calculators formerly known as the CRONUS-Earth online calculators (Balco et al., 2008). Reported *R* values are the arithmetic mean of 30 *R* values (excluding no outliers) ± the standard error of the mean.

(<5 ka) generate significantly different *R* values from those exposed during the Younger Dryas (YD), the LGM and the Würmian MIE. *R* values were recorded perpendicular to the tested surface to reduce the risk of frictional sliding of the plunger tip (Viles et al., 2011), with single impacts separated by at least a plunger width (Aydin, 2009), and no outliers were removed following Niedzielski et al. (2009). Reported *R* values are the arithmetic mean of 30 *R* values and the standard error of the mean. To account for SH drift with use (Tomkins et al., 2018), instrument calibration was based on the University of Manchester calibration boulder (Dortch et al., 2016) and performed using SHED-Earth, an online calculator developed to enable wider and more consistent application of SHED (pre–data collection: 48.27 ± 2.02; post–data collection: 48.23 ± 1.92; correction factor: 0.999).

^{10}Be exposure ages were recalibrated using the online calculators formerly known as the CRONUS-Earth online calculators (http://hess.ess.washington.edu/math/, accessed September 14, 2017, wrapper script 2.3, main calculator 2.1, constants 2.3, muons 1.1; Balco et al., 2008). Exposure ages are based on the primary calibration data set of Borchers et al. (2016), the time-dependent Lm scaling (Lal, 1991; Stone, 2000), and assuming 0 mm/ka erosion. This approach is suitable as erosion rates for most glaciated crystalline rock surfaces are usually low (0.1–0.3 mm/ka; André, 2002). Recalibrated ages must be treated as "minimum" ages because of the potential impact of surface erosion or transient shielding by snow or sediment cover. Two ^{10}Be ages are likely compromised by prior exposure (inheritance) and are excluded from further analysis. Sample CAC28 from the Cometa d'Espagne cirque (26.96 ± 2.89 ka; Crest et al., 2017) is proximal (~2 m) to three tightly clustered bedrock ages (CAC25 = 10.85 ± 2.04 ka; CAC26 = 11.97 ± 1.86 ka; CAC27 = 11.95 ± 2.92 ka; mean squared weighted deviation [MSWD] = 0.094). Similarly, sample ICM04 from the Malniu catchment (age = 80.73 ± 7.92 ka; Pallàs et al., 2010) is proximal (~10 m) to three dated moraine boulders (ICM01 = 51.12 ± 4.84 ka; ICM02 = 43.91 ± 4.28 ka; ICM03 = 42.59 ± 4.15 ka; MSWD = 0.945). Both of these data sets are internally consistent (MSWD <1; ICM01-03; CAC25-27), which suggests that prior exposure, rather than post-depositional exhumation, accounts for the positively skewed distribution of ^{10}Be ages. Remaining data (n = 52) are used to construct an ordinary least squares regression from which numerical ages can be interpolated based on SH *R* values.

To test for regional variation in rates of subaerial weathering, age control data (n = 52) were separated into subregions (Fig. 3A; southern, n = 46; eastern, n = 34; central, n = 18). These data sets were used to construct logarithmic regressions for each subregion. For each subregion regression, ages were calculated at *R* value intervals of 0.1 over the associated calibration period (southern = 4.1–51.1 ka; eastern = 10.9–51.1 ka; central = 4.1–18.2 ka). Interpolated ages were compared with the ages generated by the full age control data set, with two-sample Student's *t*-tests used to evaluate whether the difference between subregion and

https://doi.org/10.1017/qua.2018.12 Published online by Cambridge University Press

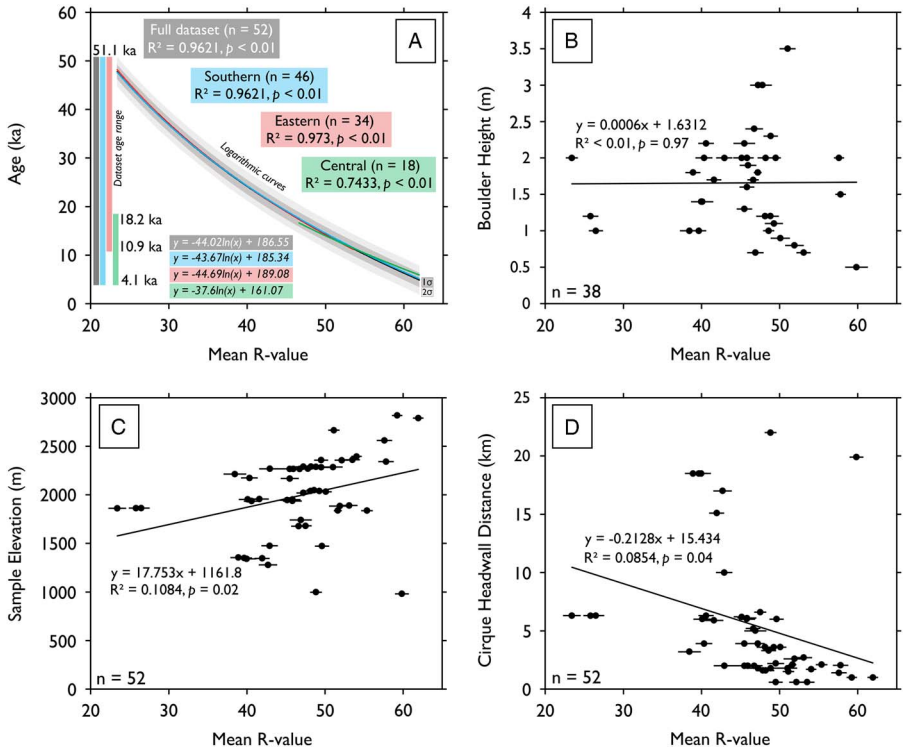

Figure 3. Local and regional controls on surface *R* values. (A) Full data set (black) and subregion calibration curves for the southern (blue), eastern (red), and central Pyrenees (green). Subregion calibration curves fall within 1σ (dark grey) and 2σ (light grey) prediction limits of the full data set curve and imply no significant variation in the rate of rock surface weathering between subregions. (B) Boulder height (m) and surface *R* values (n = 38). (C) Sample elevation (m) and surface *R* values (n = 52). (D) Cirque headwall distance (km) and surface *R* values (n = 52). These data (panels A–D) imply that site-specific factors have a negligible impact on subaerial weathering of granite surfaces in the central and eastern Pyrenees. (For interpretation of the references to colour in this figure legend, the reader is referred to the web version of this article.)

full data set results was statistically significant. Subregion information is presented in Table 2.

To verify the suitability of this TCN-SH calibration curve, 100 granite surfaces were sampled from five ice-front positions along an ~18 km transect of the Têt catchment, eastern Pyrenees (Fig. 4), with results validated against independent ^{10}Be and ^{14}C ages (Delmas et al., 2008)—that is, ^{10}Be ages that do not comprise one of the 52 age control surfaces that underpin the calibration curve (Fig. 1). Of the 26 ^{10}Be ages reported by Delmas et al. (2008), many postdate the timing of final deglaciation, likely because of moraine stabilisation processes (Hallet and Putknonen, 1994). Despite this

Table 2. Analysis of subregion data sets and comparison with the full age control data set (n = 52).

Region	Number of ages	Age range (ka)	*R*-value range[a]	Regression equation	R^2	*P* value	Mean variation[b] (ka)	Mean uncertainty[c]	Max. variation (ka)	*P* value[d]	Interpretation[e]
Full data set	52	4.1–51.1	25–60	$y = -44.02\ln(x) + 186.55$	0.96	<0.01	-	1.725 ± 0.031	-	-	-
Southern	46	4.1–51.1	25–60	$y = -43.67\ln(x) + 185.34$	0.96	<0.01	0.11 ± 0.06	1.725 ± 0.031	0.22	0.91	H_0
Eastern	34	10.9–51.1	25–54	$y = -44.69\ln(x) + 189.08$	0.97	<0.01	0.14 ± 0.08	1.728 ± 0.036	0.37	0.92	H_0
Central	18	4.1–18.2	46–60	$y = -37.6\ln(x) + 161.07$	0.74	<0.01	0.43 ± 0.22	1.704 ± 0.008	0.90	0.98	H_0

These data imply little variation in the rate of subaerial weathering between subregions.
[a]Ages interpolated at *R*-value interval of 0.1 within these ranges.
[b]Mean variation from full data set ± mean absolute deviation.
[c]Mean calibration curve uncertainty of the full data set ± mean absolute deviation over the associated calibration period.
[d]*P* value of two-sample Student's *t*-tests assuming unequal variance.
[e]H_1, the difference between the two populations is statistically significant at $P = 0.05$; H_0, the difference between the two populations is not statistically significant at $P = 0.05$.

https://doi.org/10.1017/qua.2018.12 Published online by Cambridge University Press

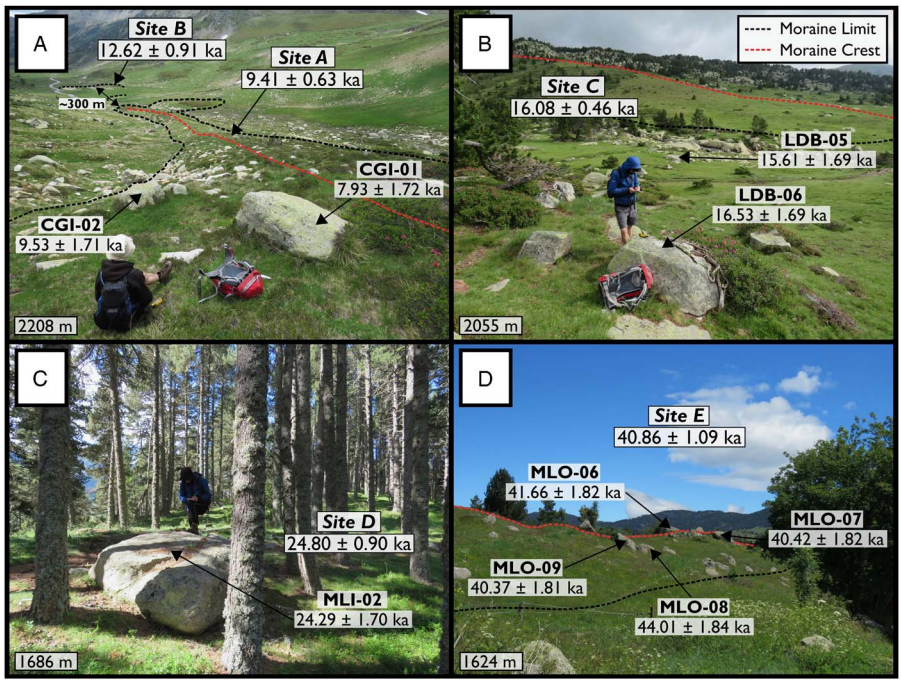

Figure 4. (colour online) Sampled sites for Schmidt hammer exposure dating (SHED) from the Têt catchment, eastern Pyrenees. (A) Holocene (site A; 9.41 ± 0.62 ka) and Younger Dryas moraines (site B; 12.62 ± 0.91 ka). (B) The prominent lateral moraine and proximal surfaces sampled for SHED (site C; 16.08 ± 0.46 ka). (C) Sampled surface from the large terminal moraine, previously dated to 24.22 ± 4.58 ka (^{10}Be, n = 1; Delmas et al., 2008), which marks the maximum extent of ice during the last glacial maximum (site D; 24.80 ± 0.90 ka). (D) The outermost moraine of Têt glacier and the Würmian maximum ice extent for this catchment (site E; 40.86 ± 1.09 ka).

limitation, these data, in addition to geomorphological mapping of moraine stages (Fig. 5), provide a useful chronological framework for ice recession in the Têt catchment and can be used as independent evidence to verify the results of SHED. Sampled sites include proximal inner (site A, 1 km from catchment headwall, ~2200 m) and outer cirque moraines (site B, 1.3 km, ~2168 m). Based on existing ^{10}Be ages, these moraines may reflect ice margin oscillations during the YD or early Holocene, although considerable age scatter (n = 5; 12.00–13.99 ka) prevents accurate separation of glacial stages. Downvalley from these sites, glacially deposited boulders adjacent to a prominent lateral moraine (site C, 5.5 km, ~2051 m) are indicative of a post-LGM readvance of Têt glacier. This site is downvalley of the Grave-amont core site, which has produced ^{14}C ages in the range 19.47–20.26 ka cal BP (n = 3). These data suggest that Têt glacier was confined to the cirque environment as early as ~20 ka. Farther south, a large terminal moraine (site D, 18.5 km, ~1686 m), dated to 24.22 ± 4.58 ka (n = 1), likely marks the LGM ice extent. ^{10}Be ages from this glacial stage exhibit considerable scatter (n = 6; 15.6–24.2 ka) and likely reflect post-depositional exhumation of moraine boulders (Hallet and Putkonen, 1994). As a result, the precise age of this landform is unclear, which limits our understanding of the dynamics of Têt glacier during the global LGM. Finally, ~300 m outside of the LGM limit, the two outermost moraines of Têt glacier (site E, 18.8 km, ~1624 m) mark the Würmian MIE, although the precise age of this landform is unclear. These moraines record the maximum extent of glaciation in the Têt catchment, as the downstream landscape is dominated by fluvial incision. These moraines are morphologically distinct from proximal LGM moraines (Delmas et al., 2008), but it is not currently clear whether these landforms were deposited synchronously, with the outer moraines subject to intense moraine stabilisation processes since the LGM, or instead, whether the outer moraines represent an earlier glacial stage (MIS 3–4; Calvet et al., 2011). At each site, 20 surfaces were sampled for SHED following the methods described previously, with SH exposure ages and 1σ uncertainties calculated using SHED-Earth (http://shed.earth/, accessed September 15, 2017; Tomkins et al., 2018). To account for geologic uncertainty, which typically displays as positive and negative skew of data sets, probability density estimates (PDEs) were produced and modelled to separate out the highest probability Gaussian distribution (Fig. 5) as per the methods of Dortch et al. (2013). Using the KS density kernel in MATLAB (2015) and a dynamic smoothing window based on age uncertainty, PDE peaks and tails were separated into individual Gaussian distributions, the sum of which integrates to the cumulative PDE at 1000 iterations to obtain the best fit. The reintegrated PDE (made from the isolated Gaussians) goodness of fit is indicated graphically (Dortch et al., 2013). Full sample information for the 100 surfaces sampled in the Têt catchment can be found in the Supplementary Materials.

https://doi.org/10.1017/qua.2018.12 Published online by Cambridge University Press

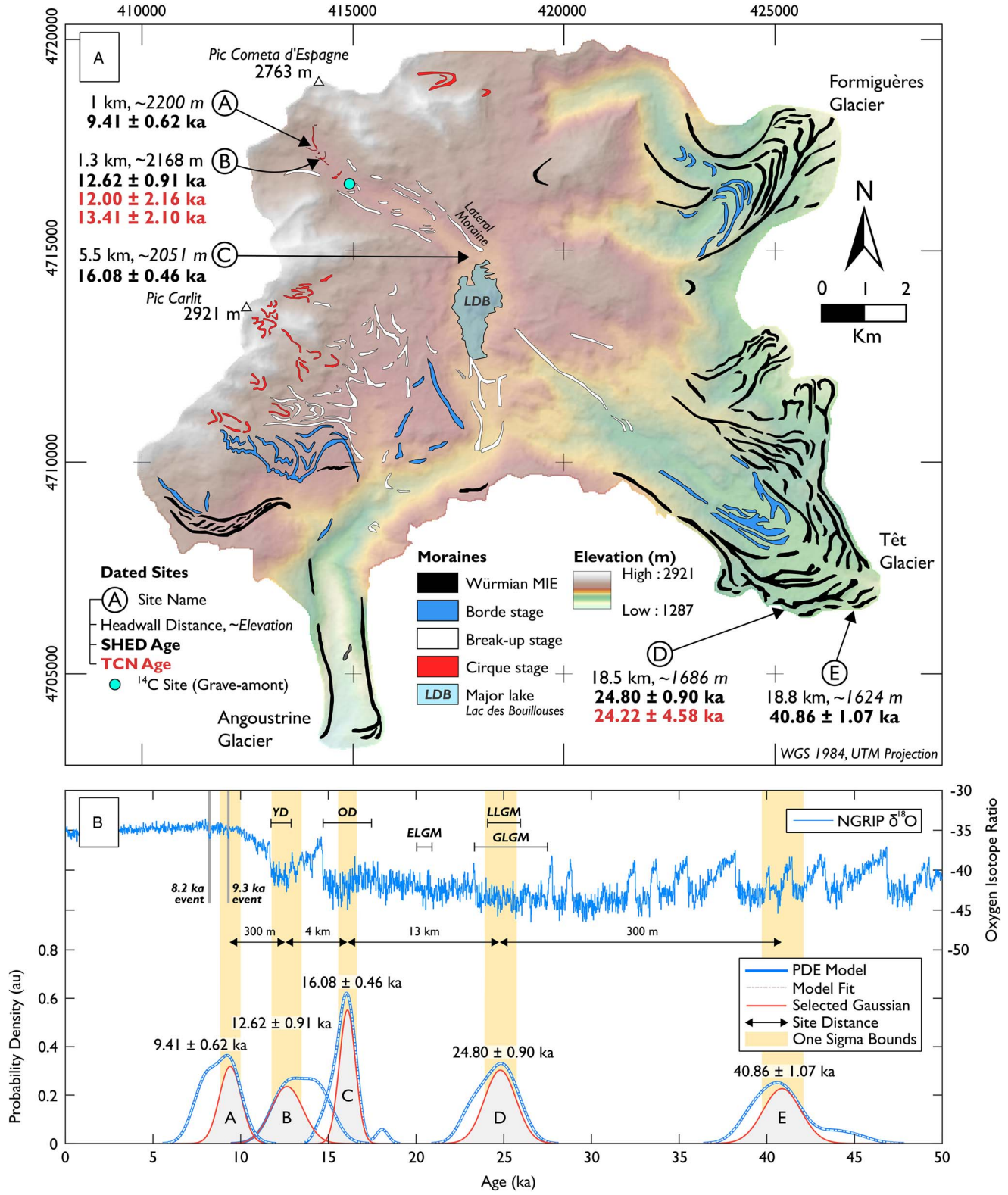

Figure 5. (colour online) A deglacial chronology for the Têt catchment, eastern Pyrenees. (A) Geomorphological map showing the Würmian maximum ice extent (MIE) for Têt, Angoustrine, and Formiguères glaciers. Moraine stages modified and terrestrial cosmogenic nuclide (TCN) exposure ages recalibrated from Delmas et al. (2008). Schmidt hammer sampled sites (Circles A–E) are shown. (B) Probability density estimates (PDEs) and Gaussian models for sampled sites. (Plots A–E) are plotted against the North Greenland Ice Core Project (NGRIP) $\delta^{18}O$ curve (Rasmussen et al., 2014). Key events are shown: Younger Dryas (YD), Oldest Dryas (OD), global last glacial maximum (GLGM), local last glacial maximum (LLGM), and the Eurasian last glacial maximum (ELGM).

https://doi.org/10.1017/qua.2018.12 Published online by Cambridge University Press

RESULTS

A clear correlation between TCN exposure ages and SH *R* values is expressed by a logarithmic regression (Fig. 1A; n = 52, $R^2 = 0.96$, $P = <0.01$). Boulder height (Fig. 3B; n = 38; $R^2 = <0.01$; $P = 0.97$), sample elevation (Fig. 3C; $R^2 = 0.11$; $P = 0.02$), and cirque headwall distance (Fig. 3D; $R^2 = 0.09$; $P = 0.04$) have a negligible correlation with *R* values. Significant differences in *R* values between recently exposed surfaces (<5 ka; *R* values >60) and those exposed during the YD (*R* values ~50), the LGM (*R* values ~40), and the Würmian MIE (*R* values ≤30) indicate that age-related information can be retained with carborundum treatment (Moses et al., 2014). There is no significant variation in subaerial weathering rate between subregions (Table 2, Fig. 3A) as eastern (n = 34), central (n = 18) and southern (n = 46) curves are completely enclosed by the 1σ boundaries of the full data set curve and generate SH ages that vary from the full data set by ≤0.37 ka, ≤0.93 ka, and ≤0.22 ka, respectively. In addition, the average subregion variation from the full data set is limited to 0.11 ± 0.06 ka and 0.14 ± 0.08 ka for the southern and eastern data sets, respectively, increasing to 0.43 ± 0.22 ka for the central data set. This likely reflects the limited calibration period (4.1–18.2 ka) and low number of age control surfaces (n = 18) for the central data set. As a result, TCN-SH calibration curves should be based on large age control data sets (≥25 ^{10}Be ages; Tomkins et al., 2016, 2018) to minimise the effect of individual exposure age errors. Despite this, two-sample Student's *t*-tests indicate that variation between age estimates derived from the full data set and southern, eastern, and central data sets is not statistically significant (Table 2; *P* values >0.91).

In the Têt catchment, SH sampling of undated glacially deposited boulders reveals statistically significant differences (two-sample Student's *t*-tests, $P < 0.01$) between the mean SH *R* values of sequential glacial landforms (A-B, B-C, C-D, D-E). Statistically significant differences in mean SH *R* values are evident between both proximal (~300 m; A-B; D-E) and distal landforms (~13 km; C-D). These data were converted into numerical ages based on the TCN-SH calibration curve presented in this article ($y = 44.02\ln(x) + 186.55$), although these must be considered minimum ages as post-depositional erosion is assumed to be negligible (0 mm/ka). Incorporating an erosion rate of 0.3 mm/ka (André, 2002) increases calibration ^{10}Be ages (n = 52) by ≤1.43% and by an average of ~0.64%, equivalent to ~0.7 ka for sample ICM01 (~50 ka) and ≤0.16 ka for surfaces exposed within the last ~25 ka. This variation is within measurement uncertainty for ^{10}Be ages and is significantly less than the 1σ uncertainty of individual SH exposure ages (minimum = 1.69 ka; maximum = 1.85 ka). As a result, incorporating erosion has a negligible impact on calculated SH exposure ages, even for landforms deposited prior to the LGM. To account for geologic uncertainty in interpolated ages, PDE modelling (Dortch et al., 2013) produces peak Gaussian distributions for glacial landforms in the Têt catchment of 9.41 ± 0.62 ka (A), 12.62 ± 0.91 ka (B), 16.08 ± 0.46 ka (C), 24.80 ± 0.90 ka (D), and 40.86 ± 1.09 ka (E).

DISCUSSION

First, a strong correlation between ^{10}Be ages and SH *R* values indicates that the primary control on surface *R* values is cumulative exposure to subaerial weathering (Tomkins et al., 2016, 2018). This correlation is observed despite marked variability in sample elevations (elevation range = ~1836 m), boulder heights (height = ~0.5 to ~3.5 m), cirque headwall distances (~0.6 to ~22 km), and relative positions along the axis of the Pyrenean mountain range (Fig. 1B; maximum distance between samples = ~110 km). These data match previous evidence from the British Isles (Tomkins et al., 2016, 2018) and the Krkonoše Mountains, Poland/Czech Republic (Engel, 2007; Engel et al., 2011), for a relationship between ^{10}Be ages and subaerial weathering of granite surfaces. However, clear differences in effective calibration time scales in the British Isles (~25 ka), the Krkonoše Mountains (~15 ka), and the Pyrenees (~50 ka) indicate that weathering rates vary significantly between these regions, likely as a function of latitudinal gradients in either precipitation or temperature. The data presented in this study also provide further evidence that weathering rates are not linear but decrease over time (White and Brantley, 2003; Stahl et al., 2013). For surfaces exposed prior to the LGM, slower rates of weathering likely reflect the formation of stable weathering residues, which slow water transport to unaltered material and impede chemical transport away from it (Colman, 1981). Finally, these data imply little variation in the rate of rock surface weathering between subregions over the last ~50 ka (Table 2, Fig. 3A). It must be noted that this interpretation is based on the assumption that recalibrated ^{10}Be ages are accurate ages for deglaciation, with no post-depositional erosion. If this assumption is not valid, then variable regional weathering rates could influence ^{10}Be ages and introduce bias to the SHED calibration curve as distal surfaces exposed synchronously could return contrasting ^{10}Be ages. However, under the assumption of minimal weathering of crystalline rock surfaces (0–3 mm/ka; André, 2002), post-depositional erosion is unlikely to have significant impact on the results of SHED as differences in ^{10}Be ages because of erosion are significantly smaller than ^{10}Be measurement uncertainty (sample ICM01; ^{10}Be age uncertainty = ± 4.99 ka; age difference 0–3 mm/ka erosion = ~0.7 ka). This appears to contrast with recent evidence from New Zealand, with marked local variability in rates of rock surface weathering (Stahl et al., 2013). This variability necessitates local calibration curves for proximal sites (~100 km distance), which are applicable over contrasting calibration time scales (Saxton and Charwell River terraces = ~10 ka; Waipara River terraces = ~1 ka; cf. Fig. 2 in Stahl et al., 2013). New data from the Pyrenees indicate that subaerial weathering of granite surfaces is consistent across the central and eastern Pyrenees, which implies that equivalent time-dependent weathering of granite surfaces can occur over significant spatial scales for regions of similar climate (Tomkins et al., 2016, 2018).

In the Têt catchment, age estimates derived from PDE modelling of Gaussian distributions (Dortch et al., 2013) are in correct stratigraphic order, are consistent with existing

https://doi.org/10.1017/qua.2018.12 Published online by Cambridge University Press

interpretations of post-MIE glaciation (Fig. 5), and are supported by independent ^{10}Be ages, which provide a chronological framework for the retreat dynamics of Têt glacier during the Würmian (Delmas et al., 2008). Gaussian ages clearly differentiate LGM (D: 24.80 ± 0.90 ka) and Würmian MIE (E: 40.86 ± 1.09 ka) glacial deposits and provide firm evidence of comparable glacier lengths during MIS 2 and MIS 3 (~300 m difference). This contrasts markedly with evidence from the western Pyrenees, where glaciers failed to reach MIE limits during the LGM (≥15 km difference; Gállego catchment; Jalut et al., 1992; Calvet et al., 2011). The proximity of MIE and LGM deposits matches the geomorphological record in Malniu (~330 m) and Querol (~600 m) and indicates that glaciers in the eastern Pyrenees advanced significantly during MIS 2 to near MIE limits, irrespective of glacier size (Querol: ~25 km; Têt: ~18.5 km; Malniu: ~6 km). A MIS 3 Würmian MIE (40.86 ± 1.09 ka) matches ages from a terminal moraine in Malniu (TCN; n = 3; 42.6–51.1 ka; Pallàs et al., 2010), a midvalley lateral moraine in the Ariege (TCN; n = 1; 37.89 ± 9.98 ka; Delmas et al., 2011), and OSL ages from the Senegüe terminal moraine in the Gállego catchment (n = 2; ~36 ka; Lewis et al., 2009). These data contrast with MIS 4 ages from ice-contact lake deposits in the Cinca catchment (OSL; n = 3; 46–71 ka; Lewis et al., 2009) and from the terminal moraine in the Ariege catchment (TCN; n = 1; 88.78 ± 18.37 ka; Delmas et al., 2011). Regardless of the precise timing of the MIE, one of the most valuable contributions of SHED is its ability to differentiate proximal LGM and MIE glacial deposits and thus enable robust comparison of glacier length fluctuations across the Pyrenees.

By comparison, the timing of the local MIS 2 glacial maximum in the Têt catchment is constrained by both TCN (n = 1; 24.22 ± 4.58 ka) and SHED ages (n = 13; 24.80 ± 0.90 ka). These data accord with recent evidence that ice masses in the European Alps reached their maximum extents at 24–26 ka because of the growth of the Laurentide Ice Sheet, which reached its maximum close to this time (>23.0 ± 0.6 ka; Ullman et al., 2015), and the southward advection of the polar front (Monegato et al., 2017). These events coincided with reduced solar radiation towards the solar minimum in the Northern Hemisphere at ~24 ka (Alley et al., 2002). In addition to SHED and TCN ages from the Têt catchment, an Alpine LGM is supported by post-maximum TCN ages from Querol (YRA samples; n = 3; 22.7–24.2 ka), the oldest ages from the frontal lobe (OEC01; 23.8 ± 2.3 ka) and a coeval lateral moraine (LAF04; 25.7 ± 2.7 ka) in Malniu (Pallàs et al., 2010), and ^{14}C ages from the Gállego catchment, which indicate that the MIS 2 MIE occurred by 24.21 ka cal BP (Jalut et al., 1992). The asynchroneity of Alpine glaciers and the Eurasian ice sheets at the global LGM, the latter reaching its maximum extent at ~21 ka (Hughes et al., 2016), demonstrates the sensitivity of Alpine ice masses to the advection of moisture from the Mediterranean Sea (Luetscher et al., 2015). The contrasting size of Pyrenean glaciers at the LGM likely reflects the relative influence of weather systems from the Atlantic and the western Mediterranean, the latter favouring cyclogenesis, convection of moist air, and increased precipitation to coastal mountain ranges (Kuhlemann et al., 2008). However, this hypothesis is tentative owing to limited geochronological data for MIS 2 glaciers in the western Pyrenees. SHED is a viable method to address this knowledge gap as the calibration curve is well constrained by age control points that span the global LGM and is able to reproduce the LGM TCN age in the Têt catchment, varying by <0.6 ka.

Finally, the geomorphological record indicates that post-LGM retreat was dynamic (Fig. 5; Borde and Cirque Stages). A number of readvance events are captured by SHED, with moraines deposited during the Oldest Dryas (OD; C: 16.08 ± 0.46 ka), YD (B: 12.62 ± 0.91 ka), and early Holocene (A: 9.41 ± 0.62 ka). Evidence for a significant readvance during the OD is matched by TCN ages from the Orri (CPM; n = 3; 16.41 ± 0.58 ka) and Malniu catchments (IMA; n = 5; 16.68 ± 0.52 ka) and is consistent with evidence for major advances in the western Pyrenees (Palacios et al., 2017). However, these data conflict markedly with ^{14}C ages from the Grave-amont core site (Fig. 5; 19.47–20.26 ka cal BP), which indicate rapid post-LGM retreat (~3.3 km/ka). New SHED data indicate that this deposit must have been overridden (Delmas et al., 2008; Crest et al., 2017). In addition, SHED clearly differentiates proximal (~300 m) YD (B: 12.62 ± 0.91 ka) and Holocene (A: 9.41 ± 0.62 ka) moraines. TCN exposure ages from the YD moraine (sample N; 12.0 ± 2.2 ka) and proximal bedrock surfaces (sample O2; 13.4 ± 2.1 ka) give contrasting age estimates but are broadly consistent with the SHED estimate. The age of the inner cirque moraine (A) overlaps with the 9.3 ka event (Rasmussen et al., 2014), although complete deglaciation and readvance of ice in the Têt catchment after the YD seems unlikely owing to the short time frame of this cooling event (~110 yr). Instead, this moraine likely marks a stillstand or readvance of the ice margin from sheltered cirques below Pic Cometa d'Espagne. These data in their totality indicate that cirque (A-B) and valley moraines (C) reflect stillstands or readvances of Têt glacier, potentially in response to North Atlantic climate fluctuations (OD, YD, 9.3 ka event). These glacial deposits provide a valuable record of ice margin fluctuations, and yet the post-LGM history of the Pyrenean ice field is currently poorly understood (Calvet et al., 2011). Future research using SHED must seek to accurately differentiate post-LGM ice masses to provide robust information on the response of these glaciers to North Atlantic climate variability.

This new SHED calibration curve demonstrates that this method can be applied successfully in contrasting climatic regimes and that equivalent time-dependent weathering of granite surfaces can occur within regions of similar climate (Tomkins et al., 2016, 2018). TCN-SH calibration curves based on significant age control data sets (n ≥ 50) have been shown to produce robust ages for glacial landforms, as demonstrated through comparison with independent radiometric ages (^{10}Be), and in aggregate, can generate results of comparable accuracy and precision to TCN dating. This

https://doi.org/10.1017/qua.2018.12 Published online by Cambridge University Press

approach could be replicated in similar well-dated granite regions throughout the world (e.g., Himalaya, Patagonia, and Sierra Nevada) and has the ability to revolutionise high-sample, low-budget quantitative studies in Quaternary science. In the Pyrenees, future applications of SHED are needed to (1) separate LGM and Würmian MIE landforms across the mountain range and (2) address gaps in our understanding of post-LGM retreat (Calvet et al., 2011). The relative scarcity of geochronological data, particularly in the western Pyrenees, has thus far prevented a Pyrenean-scale synthesis of post–MIS 4 glaciation, although progress continues to be made (e.g., Palacios et al., 2017). Widespread application of SHED across the Pyrenees would generate a wealth of new chronological data related to glacier oscillations over the last ~50 ka and would likely accelerate progress in our understanding of the last Pleistocene glacial cycle.

To apply this regional calibration curve to undated landforms or to verify its accuracy on landforms dated using radiometric methods (TCN, OSL, ^{14}C), users should follow the methods described previously and perform (1) instrument calibration and (2) age calibration procedures as described fully in Tomkins et al. (2018). To perform instrument calibration, users should sample a suitable surface before and after data collection that returns R values that lie within the range of R values measured in the field (Tomkins et al., 2018). In contrast, instrument calibration using the test anvil (R value = 81 ± 2; Proceq, 2004) is inappropriate for surfaces typically tested by Quaternary researchers (R values: 25–60) and should only be utilised for the hardest natural rock surfaces (R values ≥70). To perform age calibration and to standardise different SHs and different user strategies to the Pyrenean calibration curve, users should test their SH on one of three calibration surfaces provided (mean of 30 R values; Table 3; sample photos available at http://shed.earth) rather than the University of Manchester calibration boulder as described in Dortch et al. (2016). Users should compare the recorded mean R value against the assigned value (Table 3) to calculate a correction factor, which is then applied to all user data. This functionality is incorporated into SHED-Earth. These procedures facilitate comparison between studies and encourage wider and more consistent application of SHED throughout the Pyrenees.

Table 3. Age calibration surfaces for the Pyrenees.

Name	UTM coordinates[a]		Elevation (m)	Mean R value	SEM[b]
Maladeta calibration boulder	307424	4727841	1906	52.60	0.74
Bassies calibration boulder	374343	4733594	853	44.14	0.60
Carlit calibration boulder	422066	4707335	1820	48.67	0.65

Detailed information on age calibration can be found in Tomkins et al. (2018) or at http://shed.earth. Users should test their Schmidt hammer on one of these calibration surfaces provided (mean of 30 R values) and input their results into the SHED-Earth online calculator. Age calibration standardizes different Schmidt hammers and user strategies to the regional calibration curve.
[a]With reference to WGS 1984 31 T.
[b]SEM, standard error of the mean.

CONCLUSIONS

Quaternary deposits in the Pyrenees are ideally placed for paleoclimate studies given their proximity to both the North Atlantic and the Mediterranean. However, limited geochronological data sets, the increasing fragmentation of trunk glaciers, and the incomplete nature of the geomorphological record have prevented a regional-scale synthesis of post–MIS 4 glaciation. The Pyrenees are ideally suited for SHED given the excellent preservation of glacial deposits and the abundance of granite glacial boulders and erosion surfaces.

In this study, we show that SHED is a viable geochronological technique, as a strong correlation between 52 TCN exposure ages and SH R values ($R^2 = 0.96$, $P < 0.01$) permits the use of the SH as a numerical dating tool. The effectiveness of this method is demonstrated for the Têt catchment in the eastern Pyrenees, where SH exposure ages are in correct stratigraphic order, are consistent with existing geomorphological interpretations, and show excellent agreement with previous TCN ages. SHED data confirm comparable glacier lengths during the LGM and the MIE in the eastern Pyrenees (~300 m), in contrast to evidence from the western Pyrenees (>15 km), and also confirm the antiquity of the MIE, which likely occurred during MIS 3 (40.86 ± 1.09 ka). Moreover, SHED data show that glaciers in the eastern Pyrenees reached their maximum extents during the global LGM, synchronous with Alpine ice masses (24–26 ka). Glacier expansion was driven by enhanced moisture availability caused by southward advection of the polar front coinciding with the maximum extent of the Laurentide Ice Sheet and a solar minimum at ~24 ka.

SHED is cost and time efficient and can differentiate proximal glacial deposits (~300 m), and in aggregate, can generate results of comparable accuracy and precision to TCN dating. Moreover, our approach provides new evidence for non-linear weathering of granitic surfaces through time, likely associated with the formation of stable weathering residues. Finally, our data imply little variation in the rate of subaerial weathering between subregions over the last ~50 ka, which indicates that our calibration curve can be applied widely throughout the central and eastern Pyrenees.

ACKNOWLEDGMENTS

This project was supported by the Royal Geographical Society (with the Institute of British Geographers) with a Dudley Stamp Memorial Award and by the University of Manchester SEED Fieldwork Support Fund. MT is a recipient of a University of Manchester President's Doctoral Scholar Award and this research forms part of his PhD. JMD, PDH, and JJH would like to thank the University of Manchester Research Stimulation Fund. We would also like to

https://doi.org/10.1017/qua.2018.12 Published online by Cambridge University Press

thank Prof. John Matthews, associate editor Prof. James Shulmeister, and an anonymous reviewer for their constructive reviews.

SUPPLEMENTARY MATERIAL

To view supplementary material for this article, please visit https://doi.org/10.1017/qua.2018.12

REFERENCES

Alley, R.B., Brook, E.J., Anandakrishnan, S., 2002. A northern lead in the orbital band: north–south phasing of Ice-Age events. *Quaternary Science Reviews* 21, 431–441.

André, M.F., 2002. Rates of postglacial rock weathering on glacially scoured outcrops (Abisko-Riksgränsen Area, 68°N). *Geografiska Annaler, Series A: Physical Geography* 84, 139–150.

Aydin, A., 2009. The ISRM suggested methods for rock characterization, testing and monitoring: 2007-2014. *International Journal of Rock Mechanics and Mining Sciences* 46, 627–634.

Balco, G., Stone, J.O., Lifton, N.A., Dunai, T.J., 2008. A complete and easily accessible means of calculating surface exposure ages or erosion rates from ^{10}Be and ^{26}Al measurements. *Quaternary Geochronology* 3, 174–195.

Barr, I.D., Roberson, S., Flood, R., Dortch, J., 2017. Younger Dryas glaciers and climate in the Mourne Mountains, Northern Ireland. *Journal of Quaternary Science* 32, 104–115.

Borchers, B., Marrero, S., Balco, G., Caffee, M., Goehring, B., Lifton, N., Nishiizumi, K., Phillips, F., Schaefer, J., Stone, J., 2016. Geological calibration of spallation production rates in the CRONUS-Earth project. *Quaternary Geochronology* 31, 188–198.

Calvet, M., Delmas, M., Gunnell, Y., Bourle, D., 2011. Recent advances in research on Quaternary glaciations in the Pyrenees. In: Ehlers, J., Gibbard, P.L., Hughes, P.D. (Eds.), *Quaternary Glaciations – Extent and Chronology: A Closer Look. Developments in Quaternary Sciences*, Vol. 15. Elsevier, Amsterdam, pp. 127–139.

Cěrná, B., Engel, Z., 2011. Surface and sub-surface Schmidt hammer rebound value variation for a granite outcrop. *Earth Surface Processes and Landforms* 36, 170–179.

Colman, S.M., 1981. Rock-weathering rates as functions of time. *Quaternary Research* 264, 250–264.

Crest, Y., Delmas, M., Braucher, R., Gunnell, Y., Calvet, M., ASTER Team. 2017. Cirques have growth spurts during deglacial and interglacial periods: evidence from ^{10}Be and ^{26}Al nuclide inventories in the central and eastern Pyrenees. *Geomorphology* 278, 60–77.

Delmas, M., 2015. The last maximum ice extent and subsequent deglaciation of the Pyrenees: an overview of recent research. *Cuadernos de Investigación Geográfica* 41, 109–137.

Delmas, M., Braucher, R., Gunnell, Y., Guillou, V., Calvet, M., Bourlès, D., 2015. Constraints on Pleistocene glaciofluvial terrace age and related soil chronosequence features from vertical ^{10}Be profiles in the Ariège River catchment (Pyrenees, France). *Global and Planetary Change* 132, 39–53.

Delmas, M., Calvet, M., Gunnell, Y., Braucher, R., Bourlès, D., 2011. Palaeogeography and ^{10}Be exposure-age chronology of Middle and Late Pleistocene glacier systems in the northern Pyrenees: implications for reconstructing regional palaeoclimates. *Palaeogeography, Palaeoclimatology, Palaeoecology* 305, 109–122.

Delmas, M., Gunnell, Y., Braucher, R., Calvet, M., Bourlès, D., 2008. Exposure age chronology of the last glaciation in the eastern Pyrenees. *Quaternary Research* 69, 231–241.

Dortch, J.M., Hughes, P.D., Tomkins, M.D., 2016. Schmidt hammer exposure dating (SHED): calibration boulder of Tomkins et al. (2016). *Quaternary Geochronology* 35, 67–68.

Dortch, J.M., Owen, L.A., Caffee, M.W., 2013. Timing and climatic drivers for glaciation across semi-arid western Himalayan-Tibetan orogen. *Quaternary Science Reviews* 78, 188–208.

Engel, Z., 2007. Measurement and age assignment of intact rock strength in the Krkonoše Mountains, Czech Republic. *Zeitschrift für Geomorphologie* 51, 69–80.

Engel, Z., Traczyk, A., Braucher, R., Woronko, B., Křížek, M., 2011. Use of ^{10}Be exposure ages and Schmidt hammer data for correlation of moraines in the Krkonoše Mountains, Poland/Czech Republic. *Zeitschrift für Geomorphologie* 55, 175–196.

Gunnell, Y., Calvet, M., Brichau, S., Carter, A., Aguilar, J.-P., Zeyen, H., 2009. Low long-term erosion rates in high-energy mountain belts: insights from thermo- and biochronology in the Eastern Pyrenees. *Earth and Planetary Science Letters* 278, 208–218.

Hallet, B., Putkonen, J., 1994. Surface dating of dynamic landforms: young boulders on aging moraines. *Science* 265, 937–940.

Heyman, J., Stroeven, A.P., Harbor, J.M., Caffee, M.W., 2011. Too young or too old: evaluating cosmogenic exposure dating based on analysis of compiled boulder exposure ages. *Earth and Planetary Science Letters* 302, 71–80.

Hughes, A.L., Gyllencreutz, R., Lohne, Ø.S., Mangerud, J., Svendsen, J.I., 2016. The last Eurasian ice sheets – a chronological database and time-slice reconstruction, DATED-1. *Boreas* 45, 1–45.

Hughes, P.D., Gibbard, P.L., 2015. A stratigraphical basis for the Last Glacial Maximum (LGM). *Quaternary International* 383, 174–185.

Jalut, G., Monserrat Marti, J., Fontugne, M., Delibrias, G., Vilaplana, J.M., Julia, R., 1992. Glacial to interglacial vegetation changes in the northern and southern Pyrenees: deglaciation, vegetation cover and chronology. *Quaternary Science Review* 11, 449–480.

Katz, O., Reches, Z., Roegiers, J.-C., 2000. Evaluation of mechanical rock properties using the Schmidt Hammer. *International Journal of Rock Mechanics and Mining Sciences* 37, 723–728.

Kłapyta, P., 2013. Application of Schmidt hammer relative age dating to Late Pleistocene moraines and rock glaciers in the Western Tatra Mountains, Slovakia. *Catena* 111, 104–121.

Kuhlemann, J., Rohling, E.J., Krumrei, I., Kubik, P., Ivy-Ochs, S., Kucera, M., 2008. Regional synthesis of Mediterranean atmospheric circulation during the Last Glacial Maximum. *Science* 321, 1338–1340.

Lal, D., 1991. Cosmic ray labeling of erosion surfaces: in situ nuclide production rates and erosion models. *Earth and Planetary Science Letters* 104, 424–439.

Lewis, C.J., Mcdonald, E.V, Sancho, C., Peña, J.L., Rhodes, E.J., 2009. Climatic implications of correlated Upper Pleistocene glacial and fluvial deposits on the Cinca and Gállego Rivers (NE Spain) based on OSL dating and soil stratigraphy. *Global and Planetary Change* 67, 141–152.

Luetscher, M., Boch, R., Sodemann, H., Spötl, C., Cheng, H., Edwards, R.L., Frisia, S., Hof, F., Müller, W., 2015. North

Atlantic storm track changes during the Last Glacial Maximum recorded by Alpine speleothems. *Nature Communications* 6, 6344.

Matthews, J.A., Owen, G., 2008. Endolithic lichens, rapid biological weathering and Schmidt hammer r-values on recently exposed rock surfaces: Storbreen glacier foreland, Jotunheimen, Norway. *Geografiska Annaler, Series A: Physical Geography* 90, 287–297.

Monegato, G., Scardia, G., Hajdas, I., Rizzini, F., Piccin, A., 2017. The Alpine LGM in the boreal ice-sheets game. *Scientific Reports* 7, 1–8.

Moses, C., Robinson, D., Barlow, J., 2014. Methods for measuring rock surface weathering and erosion. *Earth-Science Reviews* 135, 141–161.

Murari, M.K., Owen, L.A., Dortch, J.M., Caffee, M.W., Dietsch, C., Fuchs, M., Haneberg, W.C., Sharma, M.C., Townsend-Small, A., 2014. Timing and climatic drivers for glaciation across monsoon-influenced regions of the Himalayan-Tibetan orogen. *Quaternary Science Reviews* 88, 159–182.

Niedzielski, T., Migoń, P., Placek, A., 2009. A minimum sample size required from Schmidt hammer measurements. *Earth Surface Processes and Landforms* 34, 1713–1725.

Ortuño, M., Martí, A., Martín-Closas, C., Jiménez-Moreno, G., Martinetto, E., Santanach, P., 2013. Palaeoenvironments of the Late Miocene Prüedo Basin: implications for the uplift of the Central Pyrenees. *Journal of the Geological Society* 170, 79–92.

Palacios, D., García-Ruiz, J.M., Andrés, N., Schimmelpfennig, I., Campos, N., Léanni, L., ASTER Team. 2017. Deglaciation in the central Pyrenees during the Pleistocene–Holocene transition: timing and geomorphological significance. *Quaternary Science Reviews* 162, 111–127.

Pallàs, R., Rodés, Á., Braucher, R., Bourlès, D., Delmas, M., Calvet, M., Gunnell, Y., 2010. Small, isolated glacial catchments as priority targets for cosmogenic surface exposure dating of Pleistocene climate fluctuations, southeastern Pyrenees. *Geology* 38, 891–894.

Pallàs, R., Rodés, Á., Braucher, R., Carcaillet, J., Ortuño, M., Bordonau, J., Bourlès., D., Vilaplana, J. M., Masana, E., Santanach, P., 2006. Late Pleistocene and Holocene glaciation in the Pyrenees: a critical review and new evidence from ^{10}Be exposure ages, south-central Pyrenees. *Quaternary Science Reviews* 25, 2937–2963.

Proceq, 2004. *Operating Instructions Betonprüfhammer N/NR- L/LR*. Proceq, Schwerzenbach, Switzerland.

Putkonen, J., Swanson, T., 2003. Accuracy of cosmogenic ages for moraines. *Quaternary Research* 59, 255–261.

Rasmussen, S.O., Bigler, M., Blockley, S.P., Blunier, T., Buchardt, S.L., Clausen, H.B., Cvijanovic, I., et al., 2014. A stratigraphic framework for abrupt climatic changes during the Last Glacial period based on three synchronized Greenland ice-core records: refining and extending the INTIMATE event stratigraphy. *Quaternary Science Reviews* 106, 14–28.

Riebe, C.S., Kirchner, J.W., Finkel, R.C., 2004. Erosional and climatic effects on long-term chemical weathering rates in granitic landscapes spanning diverse climate regimes. *Earth and Planetary Science Letters* 224, 547–562.

Stahl, T., Winkler, S., Quigley, M., Bebbington, M., Duffy, B., Duke, D., 2013. Schmidt hammer exposure-age dating (SHD) of late quaternary fluvial terraces in New Zealand. *Earth Surface Processes and Landforms* 38, 1838–1850.

Stone, J.O., 2000. Air pressure and cosmogenic isotope production. *Journal of Geophysical Research* 105, 23753–23759.

Sumner, P., Nel, W., 2002. The effect of rock moisture on Schmidt hammer rebound: tests on rock samples from Marion Island and South Africa. *Earth Surface Processes and Landforms* 27, 1137–1142.

Tomkins, M.D., Dortch, J.M., Hughes, P.D., 2016. Schmidt Hammer exposure dating (SHED): establishment and implications for the retreat of the last British Ice Sheet. *Quaternary Geochronology* 33, 46–60.

Tomkins, M.D., Huck, J.J., Dortch, J.M., Hughes, P.D., Kirkbride, M., Barr, I., 2018. Schmidt Hammer exposure dating (SHED): calibration procedures, new exposure age data and an online calculator. *Quaternary Geochronology* 44, 55–62.

Ullman, D.J., Carlson, A.E., LeGrande, A.N., Anslow, F.S., Moore, A.K., Caffee, M., Syverson, K.M., Licciardi, J.M., 2015. Southern Laurentide ice-sheet retreat synchronous with rising boreal summer insolation. *Geology* 43, 23–26.

Viles, H., Goudie, A., Grab, S., Lalley, J., 2011. The use of the Schmidt Hammer and Equotip for rock hardness assessment in geomorphology and heritage science: a comparative analysis. *Earth Surface Processes and Landforms* 36, 320–333.

White, A.F., Brantley, S.L., 2003. The effect of time on the weathering of silicate minerals: why do weathering rates differ in the laboratory and field? *Chemical Geology* 202, 479–506.

Williams, R.B.G., Robinson, D.A., 1983. The effect of surface texture on the determination of the surface hardness of rock using the Schmidt hammer. *Earth Surface Processes and Landforms* 8, 289–292.

https://doi.org/10.1017/qua.2018.12 Published online by Cambridge University Press